ACS Photonics

Article

pubs.acs.org/journal/apchd5

Incident Angle-Tuning of Infrared Antenna Array Resonances for Molecular Sensing

Tobias W. W. Maß and Thomas Taubner*

Institute of Physics (IA) and JARA - Fundamentals of Future Information Technologies, RWTH Aachen University, 52056 Aachen, Germany

Supporting Information

ABSTRACT: Nanoantenna arrays with resonances in the mid-infrared spectral range enable a high sensitivity in surface-enhanced infrared absorption spectroscopy. Commonly, multiple antenna arrays with different geometries or surrounding materials have to be fabricated in order to match and enhance different absorption bands of interest. Here, we demonstrate that, by simply changing the angle of incidence, the near-field enhancement of the antenna arrays can be spectrally tuned for maximizing sensitivity for different vibrational modes of surface molecules. Varying the incident angle spectrally shifts the rayleigh anomalies and thus the wavelengths at which collective excitation and the peak field enhancement of the antennas occur. This allows us to tune the antenna array resonance to two adjacent molecular absorption bands without changing the geometry or surrounding material of the antennas. Characteristic Fano lineshapes that alter upon changing the incident angle are observed, and the angle-dependent signal enhancement is analyzed. We gain an improvement of the absorption enhancement by a factor of up to 1.75 compared to the usual angle-averaged measurements.

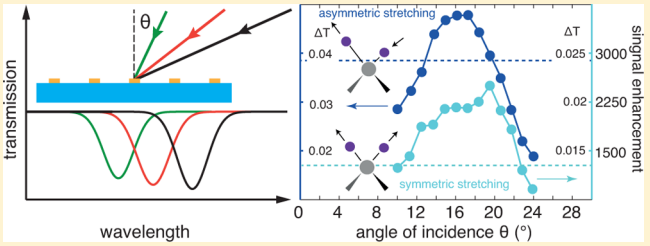

KEYWORDS: *incident angle tuning, infrared antenna array, enhanced spectroscopy*

Sensing of molecular vibrations using nano- and microstructures has been studied extensively during the last decades.[1−5] Metallic nano- and microstructures can efficiently couple light into a region of subwavelength size and enable field enhancements of several orders of magnitude.[6] This ability enables sensing of molecular vibrations with a high sensitivity and caused the expansion of both surface-enhanced Raman scattering (SERS) and infrared absorption spectroscopies (SEIRAS).[1,5,7,8] In infrared spectroscopy, the molecular absorption is proportional to the square of the local field amplitude, which can be increased by several orders of magnitude at the tip ends of infrared resonant antennas.[9,10] In order to push the sensitivity toward the detection of few or even single molecules in the mid-infrared, various routes, such as increased near-field coupling of metallic structures,[11−13] different antenna geometries,[14−17] array patterns,[18,19] and new materials[20−22] have been tackled. For SEIRA, at least monolayer sensitivity has been proven multiple times in the literature.[10,18,23] Nevertheless, a breakthrough regarding commercial applications using SEIRA substrates has not been achieved so far. Possible reasons are, that in many cases, a high sensitivity in SEIRA experiments is accompanied by a fixed, spectrally narrow range of high field enhancement, a drastically decreased volume in which these field enhancements occur or required fabrication methods that are not (yet) suitable for large-area, mass-fabrication. Commonly, the spectral position of high field enhancement is tuned and optimized to match a molecular absorption band of interest by tailoring the antenna lengths,[24,25] array periodicities,[10,18] or the refractive index of the substrate material.[25] Though these possibilities allow only little influence on the optical properties of the samples after fabrication, and in case that multiple absorption bands shall be enhanced, a higher flexibility is desirable. Regarding the active control of antenna array resonances and, thus, an increased flexibility after fabrication, improvements have been realized by using, for example, phase change materials,[26,27] electrical tuning of graphene,[1,22,28] or mechanical deformations.[29] For 1D gratings, a tuning over a broad spectral range has been shown not only by varying the period,[30] but also by changing the angle of incidence, thus, offering a high degree of flexibility.[31] Nevertheless, for 1D gratings, the peak field enhancement is lower compared to taylored nanoantennas. Ordered in an array, the performance and the maximum field enhancement of infrared antennas can be even increased by means of collective excitation, that is, when the excited charge carrier oscillations of all illuminated antennas are in phase.[18] Advantages of incident angle tuning in the visible and near-infrared spectral range have been theoretically predicted and also applied for SPR and LSPR applications like SERS.[32−36] In the mid-infrared spectral range, previous theoretical work focused on the impact of commonly used Schwarzschild objectives on antenna array performance.[37] It was shown that the performance of an infrared antenna array can be

Received: July 20, 2015
Published: September 11, 2015

DOI: 10.1021/acsphotonics.5b00399
ACS Photonics 2015, 2, 1498−1504

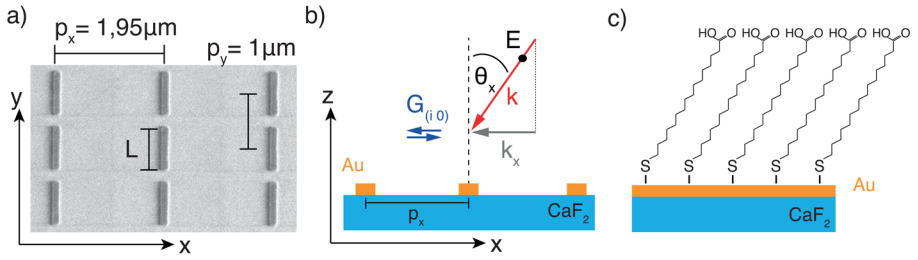

Figure 1. (a) SEM image of a part of the rod antenna array with indicated rod length L and periodicities p_x and p_y. (b) 2D sketch of perpendicular polarized light incident on the antenna arrays with indicated incident angle θ_x, in-plane k component, k_x, and reciprocal lattice vector $\vec{G}_{(i,0)}$. (c) Sketch of a self-assembled monolayer of 16-MHDA on a gold surface.

significantly reduced by the broad incident angle range inherent with this type of objective. Additionally, as focusing dielectric lenses in the mid-infrared show considerable dispersion limiting their spectral range, a more elaborate investigation about the impact of illumination angles for sensing applications is required. Here, we show the incident angle tuning of infrared antenna array resonances in order to enhance multiple absorption bands with high sensitivity. By only slightly changing the incident angle, the antenna array resonance can be shifted by around 400 wavenumbers. We observe clear changes of the Fano lineshapes when changing the spectral position of the first order rayleigh anomaly relative to the vibrational resonance frequencies. Furthermore, we improve the sensitivity compared to common angle averaged measurements by choosing an optimal angle of incidence for the given antenna array.

RESULTS AND DISCUSSION

Focused ion beam (FIB) milling is used to fabricate a rectangular ordered gold rod antenna array on a CaF_2 substrate covered with a 30 nm thick gold film. The SEM image in Figure 1a shows a small part of the 70 × 50 μm^2 sized array. The rod length is fixed to 800 nm, the width and height to 150 and 30 nm, respectively. The array periods are fixed to 1.95 μm in x- and 1 μm in y-direction. As a consequence, the gap between two antenna tips has a size of 200 nm, and therefore, the influence of near-field coupling can be neglected. After placing a self-assembled monolayer of 16-MHDA (sketched in Figure 1c), the sample is characterized via FTIR transmittance measurements using different incident angles θ of the light. For simplification, the angles θ_x and θ_y are defined as angles from the substrate normal, when regarding the projection on the x−z or y−z plane, respectively. In Figure 1b, the k_x component of the **k**-vector is perpendicular, and the electric field is parallel to the long antenna axis. The reciprocal lattice vectors are given by $\vec{G}_{(i,j)}$, where i and j are integers defining the grating order (GO). For the case depicted in Figure 1b, it counts that $j = 0$. Spectral positions of rayleigh anomalies for a 2D grating at an air/substrate interface can be derived from the Bragg coupling condition.[37] It counts that

$$\lambda_{(i,j)} = -A + \sqrt{A^2 - B} \tag{1}$$

where

$$A = \frac{\sin(\theta)}{(i/p_x)^2 + (j/p_y)^2} \cdot \left(\frac{i \sin(\phi)}{p_x} + \frac{j \cos(\phi)}{p_y} \right) \tag{2}$$

and

$$B = \frac{\sin(\theta)^2 - n^2}{(i/p_x)^2 + (j/p_y)^2} \tag{3}$$

The periodicities of the grating are p_x and p_y, n is the substrate refractive index, θ and ϕ are the polar and azimuthal angles, and i and j define the GO. Regarding an illumination direction perpendicular to the long antenna axis, as shown in Figure 1b, the equation can be simplified to

$$\lambda_{(i0)} = p_x \left(\frac{n}{|i|} - \frac{\sin(\theta_x)}{i} \right) \tag{4}$$

From eq 4 we can qualitatively state that, for a fixed grating resonance wavelength, an increase of the substrate refractive index requires a reduction of the period, but a reduction of the period p_x will also reduce the angle-induced spectral shift, in turn. Thus, CaF_2, with a comparable low refractive index around 1.4 and negligible absorption from 200 nm up to 8 μm, is chosen in order to enable large spectral shifts of GOs upon changing the angle of incidence. As an example, for an antenna array with a period p_x of about 2 μm on a CaF_2 substrate and an incident angle change from 0° to 30°, the (−1 0) CaF_2 GO resonance shifts from 2.8 to 3.8 μm. From eq 4 it is also obvious that spectral shifts of higher orders are smaller. Additionally, from the literature it is well-known that the (−1 0) substrate GO resonance has the most prominent influence on antenna array resonances.[9] Due to its spectral position, we will refer to the (−1 0) CaF_2 GO resonance as the "first GO" in the following. In case the first GO is slightly blueshifted compared to the antenna array resonance, all antennas are excited in phase. This collective excitation can cause an increase of the field enhancement at the antenna ends of about 1 order of magnitude. A significant redshift of the first GO compared to the antenna array resonance results in radiation damping and a drastic drop of field enhancement.[9] In the following we will focus on the GOs (i, 0), as the grating orders (i, j) for $j \neq 0$ are located at lower wavelengths due to the small array period in this lattice direction. Mid-infrared antenna arrays on CaF_2 are known to show a broadband antenna resonance.[11,19] This means that collective excitation and thus high field enhancement can also be tuned over a broad spectral range.

Figure 2a shows three transmittance spectra. In the following we focus on the observations and interpretations, whereas further technical details about the measurements and calculations can be found in the Supporting Information (SI). For spectrum 1 in Figure 2a, the light is incident with $\theta_x = 16°$, while spectrum 2 depicts the angle averaged case with incident angles ranging from $\theta_x = 10$−$24°$. For spectrum 3, θ_x, as well as the k_x component of the wavevector, is close to zero. Although spectrum 3 is measured with an incident angle $\theta_y = 10°$, its line

DOI: 10.1021/acsphotonics.5b00399
ACS Photonics 2015, 2, 1498−1504

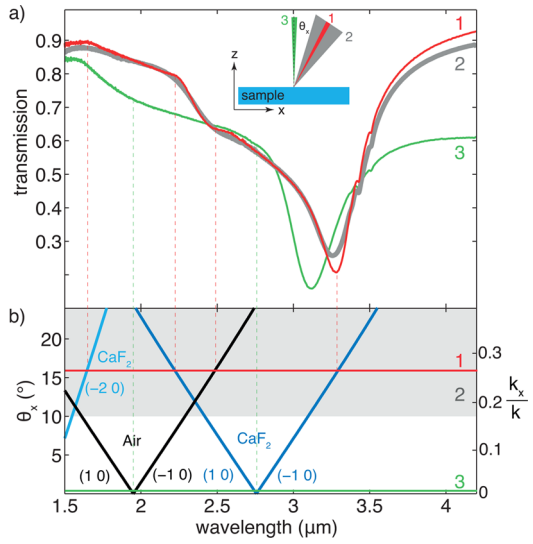

Figure 2. (a) Measured FTIR transmittance spectra: Spectrum 1, with an incident angle θ_x = 16°; Spectrum 2, with a broad angle range from θ_x = 10–24°; Spectrum 3, with θ_x = 0°, as depicted in the inset. (b) Angle dispersion of active GOs. The horizontal solid lines mark the incident angles of spectra 1 and 3, respectively. The gray area marks the angle range used in the case of spectrum 2. The vertical dashed lines are guides to the eyes and relate spectral features of the transmittance spectra in (a) to the GO dispersion in (b).

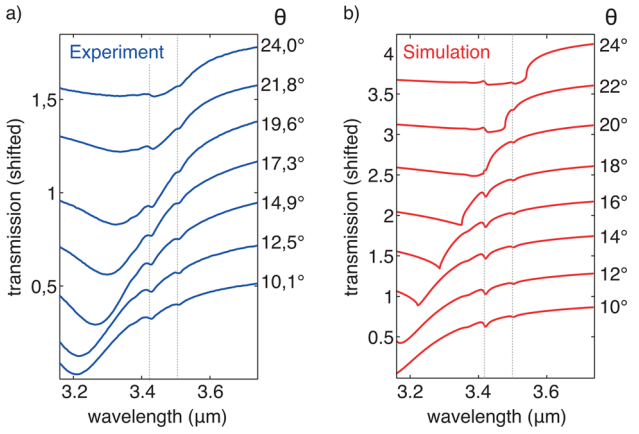

Figure 3. (a) Measured and (b) calculated angle-dependent transmittance spectra, which were vertically shifted for clarity. The incident angle θ is indicated next to the spectra. With higher incident angle, the resonance clearly redshifts and passes the spectral position of the CH_2 absorption bands marked with the vertical dashed lines.

shape approaches that of a normal incidence spectrum, as we used a different sample and polarization orientation compared to spectra 1 and 2 (see SI). At 3.4–3.5 μm, the CH_2–vibrational modes modify the line shape of the antenna array resonance. The spectra 1 and 2 are similar, as the incident angle of spectrum 1 is close to the mean value of the angle range used for spectrum 2. Nevertheless, the features of both spectra, are more prominent in the case of spectrum 1. The antenna array resonance of spectrum 3 is significantly blueshifted compared to spectrum 1, which clearly shows the angle tunability of the antenna array resonance. Most of the observations can be explained when performing a grating analysis. Figure 2b shows grating dispersions of relevant GOs calculated using eq 4. The horizontal lines mark the incident angles of spectra 1 and 3, and the gray shaded area marks the angle range of spectrum 2. The intersections of these lines with the GO dispersions mark the wavelengths at which the respective GOs become active. The dashed vertical lines are guides to the eyes and indicate that most features present in the transmittance spectra can be attributed to influences of GOs. For the angle averaged spectrum 2, the first GO is spectrally distributed from 3.08 to 3.55 μm. Thus, incident angles are included in spectrum 2 that decrease the resonance quality. For spectrum 3, the first GO is blueshifted a lot compared to spectra 1 and 2 or the vibrational bands. The resulting blueshift of the antenna array resonance is qualitatively in agreement with calculations or corresponding changes of the array periodicity shown in literature.[9,18,37] In Figure 3, measured and calculated transmittance spectra for various angles ranging from θ = 10–24° are shown. With increasing incident angle, a redshift is observed in both measurement and calculation with satisfying agreement. From Figure 2b it can be deduced that the first GO redshifts with increasing k_x. As long as the first GO is still at considerably lower wavelength than the spectral position of the antenna resonance, a redshift of the first GO will improve collective excitation, reduce the energy required to excite the antenna array, and thus, cause a redshift of the antenna resonance as well. The simulated spectra show much sharper features at wavelengths at which the first GO becomes active compared to the experimental spectra, which is due to a remaining polar (2°) and azimuthal (45°) angle range in the experiments (see SI). The vertical dashed lines mark the spectral position of the symmetric (2850 cm^{-1}) and asymmetric (2918 cm^{-1}) CH_2 vibrational bands, which are modeled by a sum of Lorentz oscillators. The strength of these oscillators is chosen according to the ratio of the absorption dips obtained by a grazing incidence reflection (GIR) reference measurement of a MHDA SAM on a flat gold surface. This GIR measurement is shown in Figure 4a, and for the symmetric and the asymmetric vibration, we measured a signal of 0.2 and 0.3%, respectively. In order to analyze the SEIRA signals obtained from molecules attached to the gold antennas, baseline fits or transmittance difference spectra of the results in Figure 3 are required. In the case of the experiments, we follow the approach presented in ref 11 and perform baseline fits, which are descibed in the SI in more detail. Some of the obtained difference spectra are shown in Figure 4b. Fano lineshapes occur as the spectrally narrow vibrational mode couples to the broad antenna resonance. When redshifting the antenna array resonance by increasing the incident angle, the coupling strength of the vibrational modes to the antenna changes. Usually, this gives rise to changes of a Fano line shape. In both simulation and experiment, we observe for the asymmetric mode a change of the Fano line shape from a minimum at 10° to a point symmetric line shape at 16–20° and finally to a maximum at 24°. For the symmetric mode, located at a higher wavelength, the Fano line shape just transforms from a minimum to point symmetric. Besides these transformations, an angle-dependent change of the vibrational absorption signal strength is already clearly observable. Finally, the very small feature at about 2875 cm^{-1} and the distinct feature at 2975 cm^{-1} should be mentioned. Spectrally, these features are close to the symmetric and asymmetric CH_3 stretch vibrations, for example, of alkanethiole SAMs on gold.[39,40] In previous SEIRA work showing the enhancement of CH_2 vibrations of ODT SAMs by resonant infrared antennas, also the asymmetric CH_3 stretch vibration of the ODT end group is observed.[10] MHDA does not provide a CH_3 group, which

DOI: 10.1021/acsphotonics.5b00399
ACS Photonics 2015, 2, 1498–1504

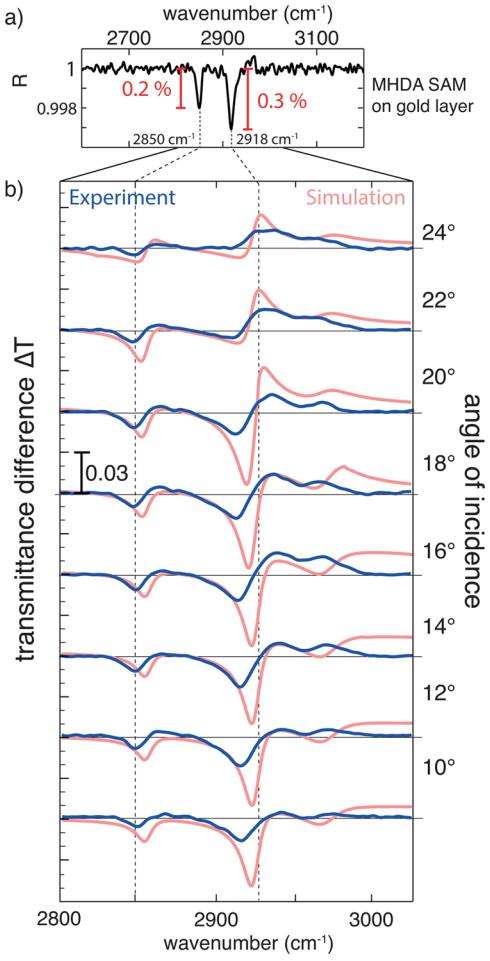

Figure 4. (a) GIR measurement of a 16-MHDA SAM on a 30 nm thick gold film. The vibrational signals of the symmetric (2850 cm^{-1}) and asymmetric (2918 cm^{-1}) modes of CH_2 yield 0.2 and 0.3%, respectively. (b) Obtained experimental (blue) and calculated (red) difference spectra for different angles of incidence. Angle-dependent changes of line shape, as well as signal strength, are clearly observed.

renders these features to be rather unexpected. As spectra with polarization along the short axis of the antennas do not reveal these molecuar vibrations, the occurrence of CH_3 is probably caused by a kind of slight contamination, which could occur either by chemical reaction after or while the monolayer forms or by residual molecules in the vicinity of the MHDA-covered antennas. Regarding the fact that the purchased MHDA powder had only 90% purity, we assume that the presence of small amounts of other molecules apart from MHDA is more likely than, for example, a chemical reaction of MHDA with the fluorite.[41] In fact, the observation of these two additional modes, especially the small feature at 2875 cm^{-1}, which is only detected at incident angles between 18° and 20°, validates our work. Without the increased sensitivity using incident angle-tuning of the antenna array resonance, this tiny feature is likely to remain undetected. The presence of other molecules brings about the question of whether these molecules increase or decrease the total number of CH_2 bonds at the antenna tips. It is not necessarily the case that more CH_2 bonds are present compared to a highly ordered, dense MHDA SAM serving as reference. This could slightly influence the enhancement factors that we examine in the following, but the incident angle dependent changes of the absorption signal enhancement remain unaffected. In the following, we will focus on the symmetric and asymmetric CH_2 vibrational bands shown in Figure 4a. In accordance with previous publications,[10,18,30] we evaluate the vibrational signal by taking the maximum and minimum value of the Fano line shape. By tuning k_x for a given frequency, we expect the near field enhancement to change continuously and to peak once the bragg coupling condition is met. For the resonance frequencies of the vibrational modes, we calculated the square of the scattered field amplitude in 5 nm distance to the tip ends of an antenna, as shown in Figure 5a. The calculated field enhancements are plotted versus the

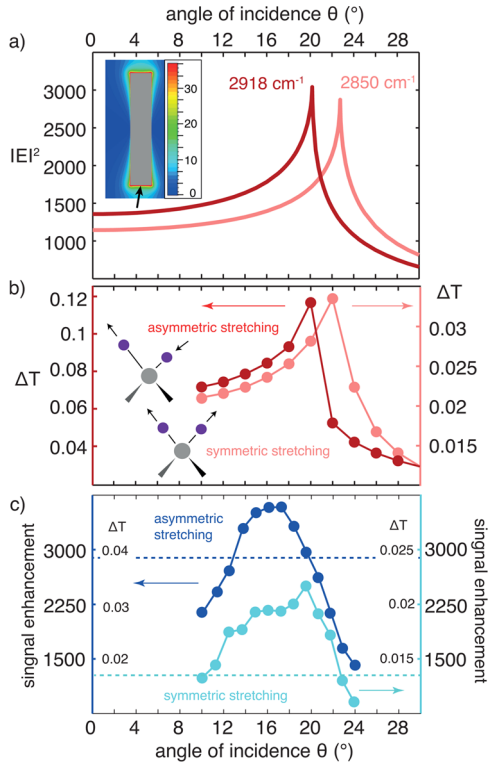

Figure 5. (a) Square of the calculated local field amplitude in close vicinity (5 nm) to the antenna ends for different incident angles. For a wavenumber of 2918 cm^{-1}, a maximum field at an angle of 20° and, for 2850 cm^{-1}, a maximum field at 22.5° are obtained. The inset exemplary shows a calculated field amplitude distribution. The black arrow points toward the position of the near-field recording. (b) Calculated vibrational signal of the symmetric (2850 cm^{-1}) and asymmetric (2918 cm^{-1}) vibrational mode from the difference spectra in Figure 4 for various incident angles. (c) Measured signal enhancement for the symmetric (2850 cm^{-1}) and asymmetric (2918 cm^{-1}) modes for various incident angles. The vertical dashed lines correspond to the enhancement obtained in the angle-averaged case.

incident angle and are comparable to values from literature.[10,18] A distinct peak of the scattered field amplitude is observed at the angles of incidence at which a collective excitation of the antenna array is realized. Accordingly, the calculated absorption signal strength is expected to peak at these angles of incidence, which is confirmed in Figure 5b. The measured transmittance differences and, accordingly, absorption signal enhancements are shown in Figure 5c. A maximum transmittance difference and thus a maximum absorption signal enhancement of 3700 at 17° incident angle is measured for the asymmetric vibration. The absorption signal enhancement of the symmetric mode peaks at a 20° incident angle with a signal enhancement of

DOI: 10.1021/acsphotonics.5b00399
ACS Photonics 2015, 2, 1498−1504

around 2500. It is important to notice that in our case the signal enhancement is calculated by referencing the SEIRA experiments to a GIR measurement of a SAM on a flat gold surface, which already enhances the molecular absorption by a factor of 16.[42,43] Regarding this, the maximum absorption signal enhancement increases to about 6×10^4 and 4×10^4 for the symmetric and asymmetric CH_2 vibrational modes, respectively. These values are in the same order as literature data, where signals of SEIRA experiments with metallic structures are referenced to a dielectric substrate.[10,18] Due to FIB milling, it is also possible that the antennas are on very small CaF_2 pedestals, which would give additional enhancement compared to antennas on a flat substrate.[44,45] Nevertheless, as the used thiol specifically binds on gold and as GIR or IRRAS measurements are a standard, conventional method for sensitive FTIR spectroscopy, we maintained it as reference for the signal enhancement calculation shown in Figure 5c. Notice the different scales for asymmetric (left) and symmetric (right) data for the transmittance difference ΔT in Figure 5b,c. The measured peak signal enhancement of the symmetric mode in Figure 5c occurs at larger incident angles compared to the asymmetric mode. This matches qualitatively well to the predictions of the calculations shown in Figure 5b, whereas the experimental curves are broadened and slightly shifted compared to the simulations. Due to radiation damping, the field enhancement drops significantly for wavelengths at which the first GO is active. This is the reason why $|E|^2$ decreases even faster for higher incident angles compared to lower angles in Figure 5a. This asymmetry in combination with the aforementioned, remaining angle ranges in the measurements could thus be a reason for the differences of simulation and experiment. The absorption signal enhancements obtained from averaged measurements are marked as dashed horizontal lines in Figure 5c. As expected, they are considerably lower compared to the peak values from the angle-resolved measurements, because unfavorable angles contribute to the average as well. For the asymmetric mode, we gain an improvement by a factor of 1.23, and for the symmetric mode, we even gained an improvement by a factor of 1.75. These improvements can be of great importance when examining features with low signal-to-noise ratio. For samples with a large area and homogeneous antenna arrays that can be illuminated with nonfocused, parallel incident light, the deviations to the simulations could be overcome and the sensitivity even increased. Especially for SEIRA experiments using mid-infrared laser sources, like, for example, quantum cascade lasers, the angle tuning of large-area metallic antenna array resonances could be realized. In case a spatial resolution is needed, the coupling of such lasers to an FTIR microscope can sustain a resolution of several micrometers,[46] and the sensitivity in our experiments can be significantly improved by introducing a pronounced near-field coupling of the antennas.[11] The gap size in our experiments remained at 200 nm, which could be easily reduced to a few tens of nanometers for future experiments. Conceptually, incident angle-tuning can also be applied in the visible or the Thz spectral range, combined with other tuning or switching mechanisms, and used for various antenna geometries.[31,35]

CONCLUSIONS

Incident angle-tuning of an infrared antenna array resonance is presented. By simply changing the angle of incidence in FTIR transmittance measurements, the near-field enhancement of the antenna arrays can be spectrally tuned for maximizing sensitivity for the symmetric and asymmetric CH_2 vibrational modes of 16-MHDA. Upon this incident angle change, the transmittance difference spectra reveal transformations of the Fano line shape from a minimum to point symmetric and to a maximum, as well as distinct variations of the absorption signal strength. When referencing to GIR measurements of a SAM on a flat gold surface and taking into account the number of contributing molecules, an optimized absorption signal enhancement of 2500 and 3700 is obtained for the symmetric and asymmetric vibrational mode, respectively. These values are increased compared to angle averaged measurements using a 15× Schwarzschild objective by factors of 1.75 for the symmetric and 1.23 for the asymmetric mode. This can be of high relevance when examining features with a low signal-to-noise ratio. Further improvements can be achieved by introducing a strong near field coupling of adjacent antennas or by an illumination with nonfocused mid-IR laser sources such as QCLs. As the incident angle-tuning is conceptually straightforward and can be extended to other wavelength ranges, our tuning approach can be combined with many other switching and tuning mechanisms that are presented in literature. This makes our work of general interest in the field of plasmonics and chemical sensing.

METHODS

Thermal evaporation is used to deposit a 30 nm thick gold layer on a CaF_2 substrate. The film thickness was in situ determined with a quartz crystal microbalance. As no lift-off process is included in the sample fabrication, there was no need for an adhesive layer. *Focused ion beam* (FIB) milling is applied in order to fabricate a gold nanoantenna array with antenna lengths of around 800 nm on a CaF_2 substrate. The used FEI Helios NanoLab DualBeam system integrates ion and electron beams for FIB and SEM functionality in one setup. This enables highly accurate navigation and milling in the few 10 nm regime. The variance of antenna lengths and positions can thus be assumed to be correspondingly small. For *FTIR transmittance measurements*, we use a Bruker Vertex 70 spectrometer and a Hyperion 2000 microscope with 15× (NA = 0.4) Schwarzschild objectives and liquid nitrogen cooled MCT detectors. The angle range of the Schwarzschild objective can be reduced by introducing home-built apertures placed between sample and objective. Generally, the spectra are recorded with polarization along the long axis of the antennas and at least 512 scans with a resolution of 2 cm^{-1}. The spectra are normalized with respect to the transmittance through the bare CaF_2 substrate. For *SAM preparation*, 16-mercaptohexadecanoic acid (90%) is purchased in order to make a 1 mM solution of 16-MHDA in ethanol. The molecules are then placed on the flat gold surface and the gold antennas by immersing the structures at least 24 h in the 1 mM solution of MHDA and ethanol. The process of monolayer formation and further details regarding the high stability of 16-MHDA in air, as well as the preparation steps, can be found elsewhere.[47,48] The *numerical simulations* have been performed with a finite integration (FIT) solver using CST Microwave Studio. A tetrahedal mesh is used and the antennas are modeled as rectangular bars. A plane wave excitation incident on the antenna array under various angles is realized by using unit cell boundaries and the Floquet Modes Port. With a postprocessing of the S-parameter results, the transmittance response can be calculated. For the near field amplitude, monitors are added in

DOI: 10.1021/acsphotonics.5b00399
ACS Photonics 2015, 2, 1498−1504

order to calculate the electric field at the vibrational frequencies of the molecules 5 nm apart from the center of the antenna tip. The molecule dielectric function is modeled as a sum of three Lorentz oscillators. The resonance position of the oscillators of the CH_2 vibrational modes are matched to the GIR reference measurements. The strength had to be increased compared to values obtained by fitting the GIR spectrum, but the relative strength of the modes is preserved. A third oscillator is introduced in order to account for the assumed, asymmetric CH_3 vibrational mode at 2975 cm^{-1}. As this mode did not show up in the reference measurement, the resonance frequency deviates slightly and this feature in the simulation is now shifted compared to the experiments. Furthermore, the molecular layer is modeled as a homogeneous, 5 nm thick layer in order to ensure a sufficient good mesh and acceptable simulation times.

■ ASSOCIATED CONTENT

Supporting Information

The Supporting Information is available free of charge on the ACS Publications website at DOI: 10.1021/acsphotonics.5b00399.

Additional analytical details and supporting Figures 6 and 7 (PDF).

■ AUTHOR INFORMATION

Corresponding Author

*E-mail: taubner@physik.rwth-aachen.de.

Notes

The authors declare no competing financial interest.

■ ACKNOWLEDGMENTS

We acknowledge financial support from the Detusche Forschungsgemeinschaft (DFG) for financial support within SPP-1327 "Sub-100 nm structures for optical and biomedical applications", which motivated this work. The authors thank the mechanical workshop of the Institute of Physics (IA) for the necessary fabrication of the home-built apertures. We thank D. N. Chigrin, J. M. Hoffmann, B. Hauer, A.-U. Michel, P. Li, L. Jung, and M. Lewin, as well as the unknown referees, for valuable comments.

■ REFERENCES

(1) Rodrigo, D.; Limaj, O.; Janner, D.; Etezadi, D.; García de Abajo, F. J.; Pruneri, V.; Altug, H. Mid-infrared plasmonic biosensing with graphene. *Science* **2015**, *349*, 165−168.

(2) Zeng, S.; Baillargeat, D.; Ho, H.-P.; Yong, K.-T. Nanomaterials enhanced surface plasmon resonance for biological and chemical sensing applications. *Chem. Soc. Rev.* **2014**, *43*, 3426−3452.

(3) Law, S.; Podolskiy, V.; Wasserman, D. Towards nano-scale photonics with micro-scale photons: the opportunities and challenges of mid-infrared plasmonics. *Nanophotonics* **2013**, *2*, 103−130.

(4) Chen, Y.; Ming, H. Review of surface plasmon resonance and localized surface plasmon resonance sensor. *Photonic Sens.* **2012**, *2*, 37−49.

(5) Aroca, R.; Ross, D.; Domingo, C. Surface-Enhanced Infrared Spectroscopy. *Appl. Spectrosc.* **2004**, *58* (11), 324−338.

(6) Novotny, L.; van Hulst, N. Antennas for light. *Nat. Photonics* **2011**, *5*, 83−90.

(7) Schlücker, S. Surface-Enhanced Raman Spectroscopy: Concepts and Chemical Applications. *Angew. Chem., Int. Ed.* **2014**, *53*, 4756−4795.

(8) Lal, S.; Grady, N. K.; Kundu, J.; Levin, C. S.; Lassiter, J. B.; Halas, N. J. Tailoring plasmonic substrates for surface enhanced spectroscopies. *Chem. Soc. Rev.* **2008**, *37*, 898−911.

(9) Adato, R.; Yanik, A. A.; Wu, C.-H.; Shvets, G.; Altug, H. Radiative engineering of plasmon lifetimes in embedded nanoantenna arrays. *Opt. Express* **2010**, *18*, 4526−4537.

(10) Neubrech, F.; Pucci, A.; Cornelius, T. W.; Karim, S.; Garcia-Etxarri, A.; Aizpurua, J. Resonant Plasmonic and Vibrational Coupling in a Tailored Nanoantenna for Infrared Detection. *Phys. Rev. Lett.* **2008**, *101* (15), 157403.

(11) Huck, C.; Neubrech, F.; Vogt, J.; Toma, A.; Gerbert, D.; Katzmann, J.; Härtling, T.; Pucci, A. Surface-Enhanced Infrared Spectroscopy Using Nanometer-Sized Gaps. *ACS Nano* **2014**, *8*, 4908−4914.

(12) Hoffmann, J. M.; Janssen, H.; Chigrin, D. N. Enhanced infrared spectroscopy using small-gap antennas prepared with two-step evaporation nanosphere lithography. *Opt. Express* **2014**, *22*, 14425−14432.

(13) Xu, X. G.; Rang, M.; Craig, I. M.; Raschke, M. B. Pushing the Sample-Size Limit of Infrared Vibrational Nanospectroscopy: From Monolayer toward Single Molecule Sensitivity. *J. Phys. Chem. Lett.* **2012**, *3*, 1836−1841.

(14) Brown, L. V.; Zhao, K.; King, N.; Sobhani, H.; Nordlander, P.; Halas, N. J. Surface-enhanced infrared absorption using individual cross antennas tailored to chemical moieties. *J. Am. Chem. Soc.* **2013**, *135*, 3688−3695.

(15) Brown, L. V.; Yang, X.; Zhao, K.; Zheng, B. Y.; Nordlander, P.; Halas, N. J. Fan-Shaped Gold Nanoantennas above Reflective Substrates for Surface-Enhanced Infrared Absorption (SEIRA). *Nano Lett.* **2015**, *15*, 1272−1280.

(16) Wu, C.; Khanikaev, A. B.; Adato, R.; Arju, N.; Yanik, A. A.; Altug, H.; Shvets, G. Fano-resonant asymmetric metamaterials for ultrasensitive spectroscopy and identification of molecular monolayers. *Nat. Mater.* **2011**, *11*, 69−75.

(17) Aouani, H.; Šípová, H.; Rahmani, M.; Navarro-Cia, M.; Hegnerová, K.; Homola, J.; Hong, M.; Maier, S. A. Ultrasensitive Broadband Probing of Molecular Vibrational Modes with Multifrequency Optical Antennas. *ACS Nano* **2013**, *7*, 669−675.

(18) Adato, R.; Yanik, A. A.; Amsden, J. J.; Kaplan, D. L.; Omenetto, F. G.; Hong, M. K.; Erramilli, S.; Altug, H. Ultra-sensitive vibrational spectroscopy of protein monolayers with plasmonic nanoantenna arrays. *Proc. Natl. Acad. Sci. U. S. A.* **2009**, *106* (46), 19227−19232.

(19) Bagheri, S.; Weber, K.; Gissibl, T.; Weiss, T.; Neubrech, F.; Giessen, H. Fabrication of Square-Centimeter Plasmonic Nanoantenna Arrays by Femtosecond Direct Laser Writing Lithography: Effects of Collective Excitations on SEIRA Enhancement. *ACS Photonics* **2015**, *2*, 779−786.

(20) Chen, Y.; Francescato, Y.; Caldwell, J. D.; Giannini, V.; Maß, T. W. W.; Glembocki, O. J.; Bezares, F. J.; Taubner, T.; Kasica, R.; Hong, M.; Maier, S. A. Spectral Tuning of Localized Surface Phonon Polariton Resonators for Low-Loss Mid-IR Applications. *ACS Photonics* **2014**, *1*, 718−724.

(21) Abb, M.; Wang, Y.; Papasimakis, N.; de Groot, C. H.; Muskens, O. L. Surface-enhanced infrared spectroscopy using metal oxide plasmonic antenna arrays. *Nano Lett.* **2014**, *14*, 346−352.

(22) Francescato, Y.; Giannini, V.; Yang, J.; Huang, M.; Maier, S. A. Graphene sandwiches as a platform for broadband molecular spectroscopy. *ACS Photonics* **2014**, *1*, 437−443.

(23) Yanik, A. A.; Cetin, A. E.; Huang, M.; Artar, A.; Mousavi, S. H.; Khanikaev, A.; Connor, J. H.; Shvets, G.; Altug, H. Seeing protein monolayers with naked eye through plasmonic Fano resonances. *Proc. Natl. Acad. Sci. U. S. A.* **2011**, *108*, 11784−11789.

(24) Neubrech, F.; Kolb, T.; Lovrincic, R.; Fahsold, G.; Pucci, A.; Aizpurua, J.; Cornelius, T. W.; Toimil-Molares, M. E.; Neumann, R.; Karim, S. Resonances of individual metal nanowires in the infrared. *Appl. Phys. Lett.* **2006**, *89*, 253104.

(25) Hoffmann, J. M.; Yin, X.; Richter, J.; Hartung, A.; Maß, T. W. W.; Taubner, T. Low-Cost Infrared Resonant Structures for Surface-Enhanced Infrared Absorption Spectroscopy in the Fingerprint Region from 3 to 13 μm. *J. Phys. Chem. C* **2013**, *117*, 11311−11316.

(26) Michel, A.-K. U.; Chigrin, D. N.; Maß, T. W. W.; Schönauer, K.; Salinga, M.; Wuttig, M.; Taubner, T. Using low-loss phase-change

DOI: 10.1021/acsphotonics.5b00399
ACS Photonics 2015, 2, 1498−1504

materials for mid-infrared antenna resonance tuning. *Nano Lett.* **2013**, *13*, 3470−3475.
(27) Michel, A.-K. U.; Zalden, P.; Chigrin, D. N.; Wuttig, M.; Lindenberg, A. M.; Taubner, T. Reversible Optical Switching of Infrared Antenna Resonances with Ultrathin Phase-Change Layers Using Femtosecond Laser Pulses. *ACS Photonics* **2014**, *1*, 833−839.
(28) Emani, N. K.; Chung, T.-F.; Ni, X.; Kildishev, A. V.; Chen, Y. P.; Boltasseva, A. Electrically Tunable Damping of Plasmonic Resonances with Graphene. *Nano Lett.* **2012**, *12*, 5202−5206.
(29) Pryce, I. M.; Kelaita, Y. A.; Aydin, K.; Atwater, H. A. Compliant Metamaterials for Resonantly Enhanced Infrared Absorption Spectroscopy and Refractive Index Sensing. *ACS Nano* **2011**, *5*, 8167−8174.
(30) Wang, T.; Nguyen, V. H.; Buchenauer, A.; Schnakenberg, U.; Taubner, T. Surface enhanced infrared spectroscopy with gold strip gratings. *Opt. Express* **2013**, *21*, 9005−9010.
(31) Petefish, J. W.; Hillier, A. C. Angle-Tunable Enhanced Infrared Reflection Absorption Spectroscopy via Grating-Coupled Surface Plasmon Resonance. *Anal. Chem.* **2014**, *86*, 2610−2617.
(32) Pinchuk, A. O. Angle Dependent Collective Surface Plasmon Resonance in an Array of Silver Nanoparticles. *J. Phys. Chem. A* **2009**, *113*, 4430−4436.
(33) Hao, F.; Sonnefraud, Y.; Dorpe, P. V.; Maier, S. A.; Halas, N. J.; Nordlander, P. Symmetry Breaking in Plasmonic Nanocavities: Subradiant LSPR Sensing and a Tunable Fano Resonance. *Nano Lett.* **2008**, *8*, 3983−3988.
(34) Hao, F.; Nordlander, P.; Sonnefraud, Y.; Dorpe, P. V.; Maier, S. A. Tunability of Subradiant Dipolar and Fano-Type Plasmon Resonances in Metallic Ring/Disk Cavities: Implications for Nanoscale Optical Sensing. *ACS Nano* **2009**, *3*, 643−652.
(35) Yu, C.-C.; Tseng, Y.-C.; Su, P.-Y.; Lin, K.-T.; Shao, C.-C.; Chou, S.-Y.; Yen, Y.-T.; Chen, H.-L. Incident angle-tuned, broadband, ultrahigh-sensitivity plasmonic antennas prepared from nanoparticles on imprinted mirrors. *Nanoscale* **2015**, *7*, 3985−3996.
(36) Baumberg, J. J.; Kelf, T. A.; Sugawara, Y.; Cintra, S.; Abdelsalam, M. E.; Bartlett, P. N.; Russell, A. E. Angle-Resolved Surface-Enhanced Raman Scattering on Metallic Nanostructured Plasmonic Crystals. *Nano Lett.* **2005**, *5*, 2262−2267.
(37) Liberman, V.; Adato, R.; Mertiri, A.; Yanik, A. A.; Chen, K.; Jeys, T. H.; Erramilli, S.; Altug, H. Angle-and polarization-dependent collective excitation of plasmonic nanoarrays for surface enhanced infrared spectroscopy. *Opt. Express* **2011**, *19*, 11202−11212.
(38) Frey, B. L.; Corn, R. M. Covalent Attachment and Derivatization of Poly(L-lysine) Monolayers on Gold Surfaces As Characterized by Polarization-Modulation FT-IR Spectroscopy. *Anal. Chem.* **1996**, *68*, 3187−3193.
(39) Hu, Z. G.; Prunici, P.; Patzner, P.; Hess, P. Infrared Spectroscopic Ellipsometry of n-Alkylthiol (C5-C18) Self-Assembled Monolayers on Gold. *J. Phys. Chem. B* **2006**, *110*, 14824−14831.
(40) Laibinis, P. E.; Whitesides, G. M.; Allara, D. L.; Tao, Y. T.; Parikh, A. N.; Nuzzo, R. G. Comparison of the Structures and Wetting properties of Self-Assembled Monolayers of n-Alkanethiols on the Coinage Metal Surfaces, Cu, Ag, and Au. *J. Am. Chem. Soc.* **1991**, *113*, 7152−7167.
(41) Weber, D. Nanogaps for Nanoantenna-Assisted Infrared Spectroscopy. *Ph.D. Thesis*, University of Heidelberg, Heidelberg, Germany, 2011.
(42) Berreman, D. W. Infrared Absorption at Longitudinal Optic Frequency in Cubic Crystal Films. *Phys. Rev.* **1963**, *130*, 2193−2198.
(43) Pucci, A. IR spectroscopy of adsorbates on ultrathin metal films. *Phys. Status Solidi B* **2005**, *242*, 2704−2713.
(44) Huck, C.; Toma, A.; Neubrech, F.; Chirumamilla, M.; Vogt, J.; De Angelis, F.; Pucci, A. Gold Nanoantennas on a Pedestal for Plasmonic Enhancement in the Infrared. *ACS Photonics* **2015**, *2*, 497−505.
(45) Cetin, A.; Etezadi, D.; Altug, H. Accessible Nearfields by Nanoantennas on Nanopedestals for Ultrasensitive Vibrational Spectroscopy. *Adv. Opt. Mater.* **2014**, *2* (9), 866−872.
(46) Steinle, T.; Neubrech, F.; Steinmann, A.; Yin, X.; Giessen, H. Mid-infrared Fourier-transform spectroscopy with a high-brilliance tunable laser source: investigating sample areas down to 5 μm diameter. *Opt. Express* **2015**, *23*, 11105−11113.
(47) Peng, D. K.; Lahann, J. Chemical, Electrochemical, and Structural Stability of Low-Density Self-Assembled Monolayers. *Langmuir* **2007**, *23*, 10184−10189.
(48) Mendoza, S. M.; Arfaoui, I.; Zanarini, S.; Paolucci, F.; Rudolf, P. Improvements in the Characterization of the Crystalline Structure of Acid-Terminated Alkanethiol Self-Assembled Monolayers on Au(111). *Langmuir* **2007**, *23*, 582−588.

DOI: 10.1021/acsphotonics.5b00399
ACS Photonics 2015, 2, 1498−1504